

Orbit to Ground Framework to Decode and Predict Biosignature Patterns in a Martian Analog

Kimberley Warren-Rhodes^{1,2}, Nathalie A. Cabrol¹, Michael Phillips³, Cinthya Tebes Cayo⁴, Freddie Kalaitzis⁵, Diego Ayma⁴, Cecilia Demergasso⁴, Guillermo Chong-Diaz⁴, Kevin Lee⁶, Nancy Hinman⁷, Kevin L. Rhodes⁸, Linda Ng Boyle⁹, Janice L. Bishop¹, Michael H. Hofmann⁷, Neil Hutchinson¹⁰, Camila Javiera⁴, Jeffrey Moersch³, Claire Mondro³, Nora Nofke¹¹, Victor Parro¹², Connie Rodriguez⁴, Pablo Sobron^{1,13}, Philippe Sarazzain¹, David Wettergreen¹⁴, Kris Zacny¹⁵ and the SETI Institute NAI Team.

1. SETI Institute Carl Sagan Center, 169 Bernardo Avenue, Suite 200. Mountain View, CA, USA.
2. NASA Ames Research Center, Space Science Division and Astrobiology Division, Moffett Field, CA, USA.
3. Johns Hopkins, Applied Physics Laboratory, Laurel, MD, USA.
4. Universidad Católica del Norte, Antofagasta, Chile.
5. Department of Computer Science, University of Oxford, UK.
6. Auckland University of Technology, Auckland, NZ.
7. Department of Geosciences, University of Montana, Missoula, MT, USA.
8. MarAlliance, San Francisco, USA.
9. University of Washington, Seattle, WA, USA.
10. Tropical Futures Institute, James Cook University, Singapore.
11. Old Dominion University, Norfolk, VA, USA.
12. Centro de Astrobiología (INTA-CSIC), Madrid, Spain.
13. Impossible Sensing, St. Louis, MO, USA.
14. Carnegie Mellon University Robotics Institute, Pittsburgh, PA, USA.
15. Honeybee Robotics, Altadena, CA, USA.

Key words: Biosignature, Mars, deep learning, habitability, endolith, biological soil crust, landscape ecology, astrobiology, convolutional neural network, artificial intelligence, machine learning, model, algorithm, rover, search, detection

- Address correspondence to: krhodes@seti.org

Bold paragraph

We advance an adaptable framework that couples statistical ecology with deep learning to recognize and predict biosignature spatial patterns in a polyextreme terrestrial environment. Drone flight imagery connected simulated HiRISE imagery to ground surveys, spectroscopy and biosignature mapping to reveal predictable distributions linked to environmental factors. AI/ML models successfully identified geologic features with high probabilities for containing biosignatures at spatial scales relevant to rover-based astrobiology exploration. Targeted approaches augmented by deep learning delivered 56.9-87.5% probabilities of biosignature detection versus <10% for random searches and reduced the physical search space by 85-97%. Libraries of biosignature distributions, detection probabilities, predictive models and search roadmaps for many terrestrial environments will standardize analog science research, enabling agnostic comparisons at all scales. This is vital to preparing, informing and optimizing biosignature quests on Mars, assisting high-stakes mission decisions between competing targets, and maximizing precise selection of high-priority samples.

In extreme environments, the distribution of biosignatures is tightly controlled by a complex interdependency of geological, physicochemical, and biological interactions¹⁻⁵. In such environments, microbial populations often occur in non-random spatial distributions closely tied to their

physical settings, key morphologies (substrates, ‘habitats’) and/or requirements for life, especially water⁶⁻¹⁰. To date, few studies have systematically examined such linkages across integrated spatial scales (Fig. 1) or tested the predictive power and probabilities of detecting life at the extremes of habitability¹¹⁻¹³. In this Article, we present a proof-of-concept study that quantifies such probabilities and constructs the first predictive astrobiology models for geologic feature recognition and biosignature detection.

Our process combines statistical microbial landscape ecology^{14,15} with remote sensing from unmanned aerial vehicles (UAV/drone) and machine learning to map and explain (Figs. 2-3), model and predict (Figs. 4-5) the distributions of biosignatures in a Mars-relevant evaporitic paleolake setting. Our approach captures microbial spatial distributions and their controls across a continuum of scales and demonstrates that, even amidst near-uniform mineralogy, biosignature patterns are discernible, non-random and predictable. We improve the probability of detecting biosignatures¹³ from <10% (for random search) to up to 87.5% by augmenting macro and microhabitat targeting with deep learning. Simultaneously, we shrink the search space by up to 97%. Ultimately, our goal is to provide a broadly applicable and adaptable methodological framework to standardize terrestrial analog research. With this approach, the astrobiology community can build a database, akin to spectral libraries, of biosignature distributions, detection probabilities, and predictive models to guide and inform Mars exploration¹⁶⁻¹⁹.

Biosignatures in Salar de Pajonales Occur in Non-Random Patches Controlled by Habitat-Type and Water

We quantified the distribution of photosynthetic communities in Salar de Pajonales (Pajonales), a 104 km² ancient lakebed located at 3,500 m elevation at the margin of the hyperarid Atacama Desert and Chilean Altiplano (Fig. 1).²⁰ Exceptionally high UV radiation²¹, hypersalinity and cold temperatures distinguish Pajonales as an analog for the evaporitic basins of Mars. Polyextreme conditions pose serious challenges for life but complex microbial populations can inhabit and have high potential to be preserved in salt crusts and sediments^{16, 22-24}. These properties make salt-encrusted basins and their microbiomes ideal terrestrial analogs to map extant or extinct biosignatures and promising future targets for missions to Mars.¹⁶⁻¹⁸.

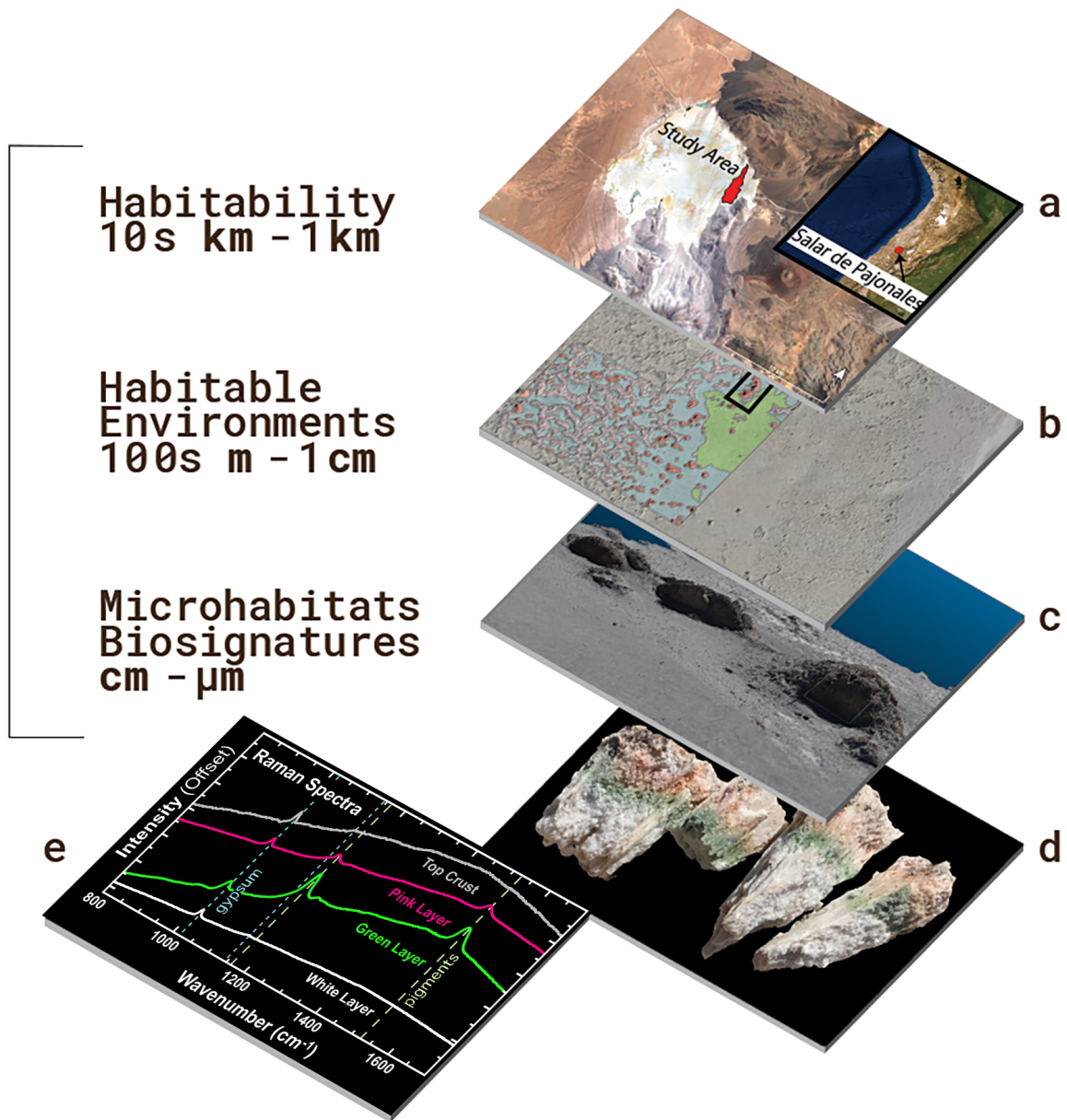


Fig. 1. Orbit-to-ground Scales of Investigation. **a**, Orbital view of Salar de Pajonales, Chile. The study area (8,193 m^2), composed of a field of gypsum domes, is shown in red. **b**, UAV view of the Dome Field in the southern portion of the Pajonales location, the focus of this study, with macrohabitats shown in false color: domes: red; ridges/polygonal networks: pink; aeolian cover: blue; patterned ground: green. The black box delineates the dome complex for the fine-scale study. **c**, Detail of the fine-scale study area with the 3D representation of dome macrohabitats obtained from drone imaging, comparable to a rover “MastCam” scale. **d**, Colored bands (biosignatures) of endolithic photosynthetic communities colonizing a gypsum Type II crystal microhabitat in the domes and **e**, Raman spectra of the distinct biosignature layers from **d**, comparable to “SuperCam” Raman spectra on the Mars 2020 rover Perseverance.

Pajonales exhibits features from both physical and biological processes highly relevant to biosignature search on Mars²⁰. Fractal-like ridge networks, patterned ground and shrinkage crack

terrains of abiotic and/or biotic origin (Extended Data Fig. 1) are morphologically similar to the polygonal terrain observed from orbit in salt-encrusted basins on Mars ^{20,25}. The Pajonales paleo-lake basin contains hydrated Ca-sulfate and chloride minerals and modern and fossilized stromatolite and microbialite formations that serve as protective refugia for soil crust or endolithic assemblages ²⁶⁻²⁹ (Extended Data Fig. 1). These sulfate-chloride habitats have high-to-very high preservation potential and are cousins to the better studied “microbial structures, textures and microfossils preserved in carbonates, silica and clay-rich deposits” ³⁰⁻³¹.

At Pajonales, we studied a 2.78 km² landscape of surficial polygonal networks and domical structures (‘Dome Field’) composed of near-uniform mineralogy (gypsum, CaSO₄•2H₂O). ²⁰ Landscape morphology was classified and quantified by UAV and with five *in situ* nested random ecological studies (Methods, Extended Data Fig. 2, Extended Data Tables 1-2, Supplementary Fig. 1). The presence/absence of biosignatures was characterized with standard visual assessments (7,765 images, n=1,154 random samples) of two distinct biological morphotypes comprising photosynthetic microorganisms: 1) endolithic colonization, i.e. layered communities within salt structures ²³; and 2) biological soil crusts ^{2,32} (BSC), i.e. occupying surficial habitats (Extended Data Fig. 1). Raman and Visible Short-Wave Infrared (VSWIR) spectroscopy, multiplex microarray immunoassays and 16S rRNA gene sequencing of pigmented samples revealed distinctive markers for life. Markers included carotenoid biosignatures expressed as orange-pink layers produced by halophilic, radiation- and desiccation-resistant bacteria and archaea and chlorophyll biosignatures, as green layers produced by cyanobacteria (Extended Data Fig. 1). In all samples, absorption features in the reflectance spectra corresponded to biosignatures in the green and orange-pink endolithic bands.

Biotic abundance was quantified as the probability of colonization, defined as percent colonization (%Col = number of samples with biosignatures of photosynthetic communities ÷ total number of samples x 100, See Methods). Assessments were validated by VSWIR and Raman spectroscopy, microscopy, mass spectroscopy, genomics and proteomics (See Methods, Extended Data, and Supplementary Fig. 2). Mineralogy and geochemistry were assessed in the field by VSWIR and in the laboratory by X-ray diffraction (XRD) and micro X-ray fluorescence spectroscopy (See Methods).

Biosignatures Cluster by Spatial Scale and Macro and Microhabitat

The spatial distribution of microbial biosignatures at Pajonales varied significantly. Specifically, 9.2% of the location was colonized, with communities clustered in isolated, non-random spatial patterns (Fig. 2, Extended Data Table 2, Supplementary Data Fig. 3).

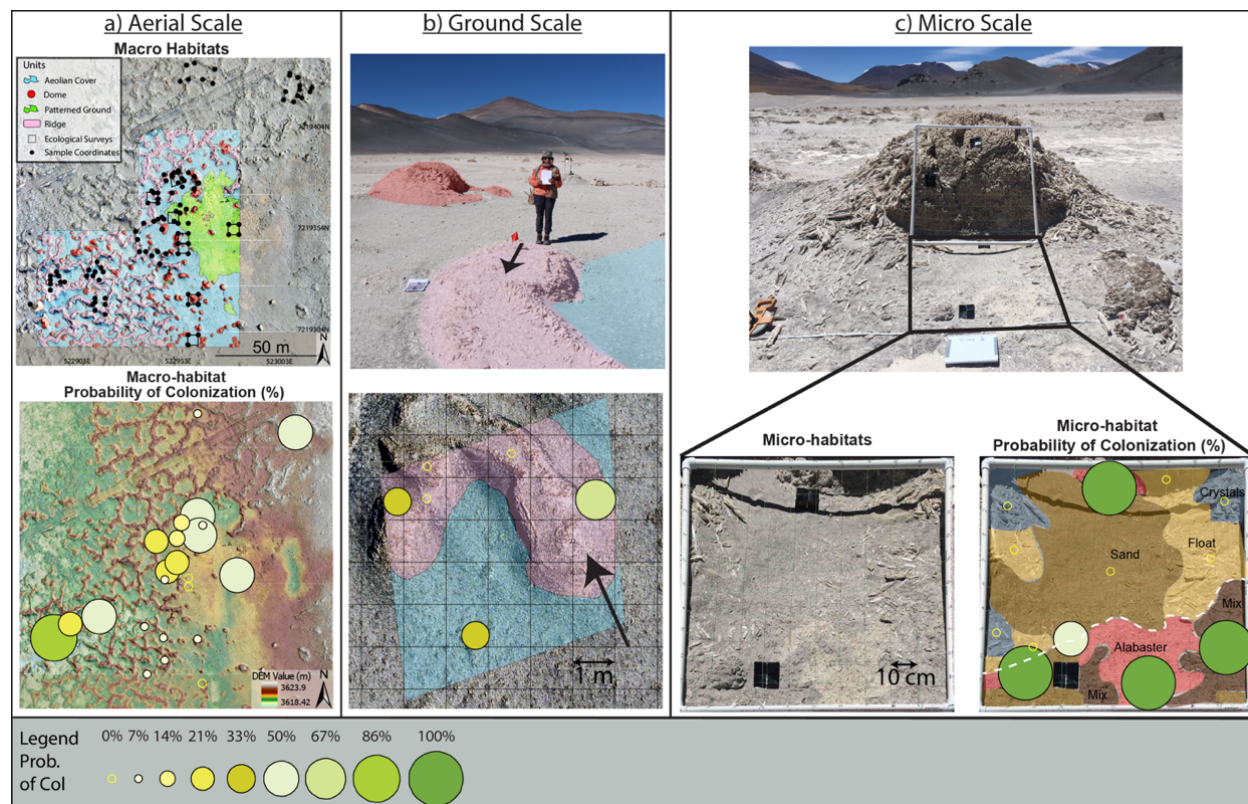


Fig. 2. Biosignatures exhibit significant spatial heterogeneity and occur in non-random clustered distributions at hierarchical scales. **a, top,** Aerial view of Dome Field macrohabitats in UAV false color: Domes (red), Ridges/polygonal networks (pink), Aeolian cover (blue), and patterned ground (green). Black squares show eight randomly selected survey areas (5 m x 5 m); black dots show individual sample sites (See Methods; Extended Data Fig. 2 and Tables 1,2; Supplementary Figs. 1,3); **a, bottom,** spatial survey results (e.g., areas, quadrants, Extended Data Table 2) for probability of colonization (as presence/absence of biosignatures, i.e., percent colonization, %Col, circles) for pigmented endolithic and BSC communities; **b, top,** Visible image of dome, ridge and aeolian cover macrohabitats at ground scale; **b, bottom,** example of spatial survey results for study area #35 of quadrant 6; each %Col circle is a 'site' mean of three random 10-cm² 'microsite' spatial replicates (ES-1, Extended Data Fig. 2). The black arrow indicates the same perspective as in **b, top** image; **c, top,** close-up image of dome visible in **b**, the site of the fine-scale ES-3 study (n=800 samples; white and black boxes are 1-m² quadrats; Extended Data Fig. 2); **c, bottom left,** close-up visible image of microhabitats; Biosignature mapping results (red: alabaster; brown: sand; tan: float; blue-grey: crystals) in same visible image are shown in **c, bottom right,** with %col for each microhabitat. Note the microbial hotspots near the microscale habitat transition zone outlined by white dashed line. Black tiles ground-truthed HySpex Mjölnir spectral scans.

UAV and ground survey data classified geomorphological features into four macrohabitats (m-to-km scales) and six microhabitats (cm-scale), each with distinct biosignature probabilities (Table

1, Fig. 3). Every dome supported at least one endolithic biosignature, with a mean probability across all dome samples of 40.8% (Table 1, Extended Data Table 2). Ridges and aeolian cover had significantly lower colonization. Patterned ground covered 40.3% of the study area's salar surface, with 50% colonized by BSC (Table 1, Fig. 3).

Table 1. Macro and microhabitats exhibit significantly different probabilities for containing endolithic or biological soil crust (BSC) biosignatures.

Surface Geomorphological Features/MacroHabitats ⁽¹⁾			Probability of Biosignatures
Habitat Type	Dimensions	Description	(%Col) ⁽²⁾
Domes	1-7.5 m, ≤ 20 cm thick crust	Sub-circular, convex-upward, hollow; tumuli ³³ ; topographic highs (~ 0.1 -2.0 m); 8.7% of total surface area of study location (8,193 m ²)	40.8%
Ridges (or Polygon Ridges)	1-100s m long	Continuous topographic gypsum features (height 0.1-1.87 m); ridges are the exteriors of large-scale polygonal networks (diameter: 5-15 m); 28.2% of total surface area; 'polygon ridges' or 'pressure ridges' ³³	18.4%
Aeolian (Surface) Cover	Salar-wide	Gypsum regolith comprising intermixed gypsum grains (silt to sand-sized) and wind-blown volcanic grains; 48.5% of total surface area of study location; quasi-flat aeolian surface cover comprises the interior of large-scale polygonal networks	10.2%
Patterned Ground	Salar-wide	Bare gypsum quasi-flat surface covered by microstructures (height 1-3 cm); fractal-like patterned ground (Fig. 3a, green) among other habitat types (Fig. 3a, blue, pink, red); 14.5% of total surface area	50%
MicroHabitats (≤ 10 cm ²) ⁽³⁾			
Alabaster	$< 200 \mu\text{m}$	Powdery, finely crystalline gypsum with abundant inter-crystalline pores within domes, ridges and aeolian cover	87.5%
Crystals	< 18 cm	Large gypsum crystals (selenite) with abundant inter-crystalline pores within domes, ridges and aeolian cover	15.7%
Float	< 10 cm	Mixture of loose sand and eroded crystals, typically lying horizontally on the surface	0%
Sand	< 2 mm	Gypsum grains (locally mixed with quartz, feldspar, hematite, magnetite grains)	0% ⁽⁴⁾
Bare salar surface	NA	Flat-lying surface with gypsum crystals (001) oriented perpendicular to the surface; interiors of micropolygons	0%
Microstructures	< 2 cm	Narrow, sinuous networks of cemented, finely crystalline gypsum with positive relief; rims of micropolygons	100%

1) Detected in drone and simulated satellite imagery and characterized with VSWIR and Raman spectroscopy. 2) Probability of biosignatures, as percent colonization (%Col; χ^2 tests and detailed statistics, see Extended Data Table 2 and Supplementary Tables 1-3). 3) Detected *in situ* in ground surveys and analyzed via VSWIR and Raman spectroscopy in the field and laboratory. 4) Sand %Col ranged from 0-7% (Extended Data Table 2).

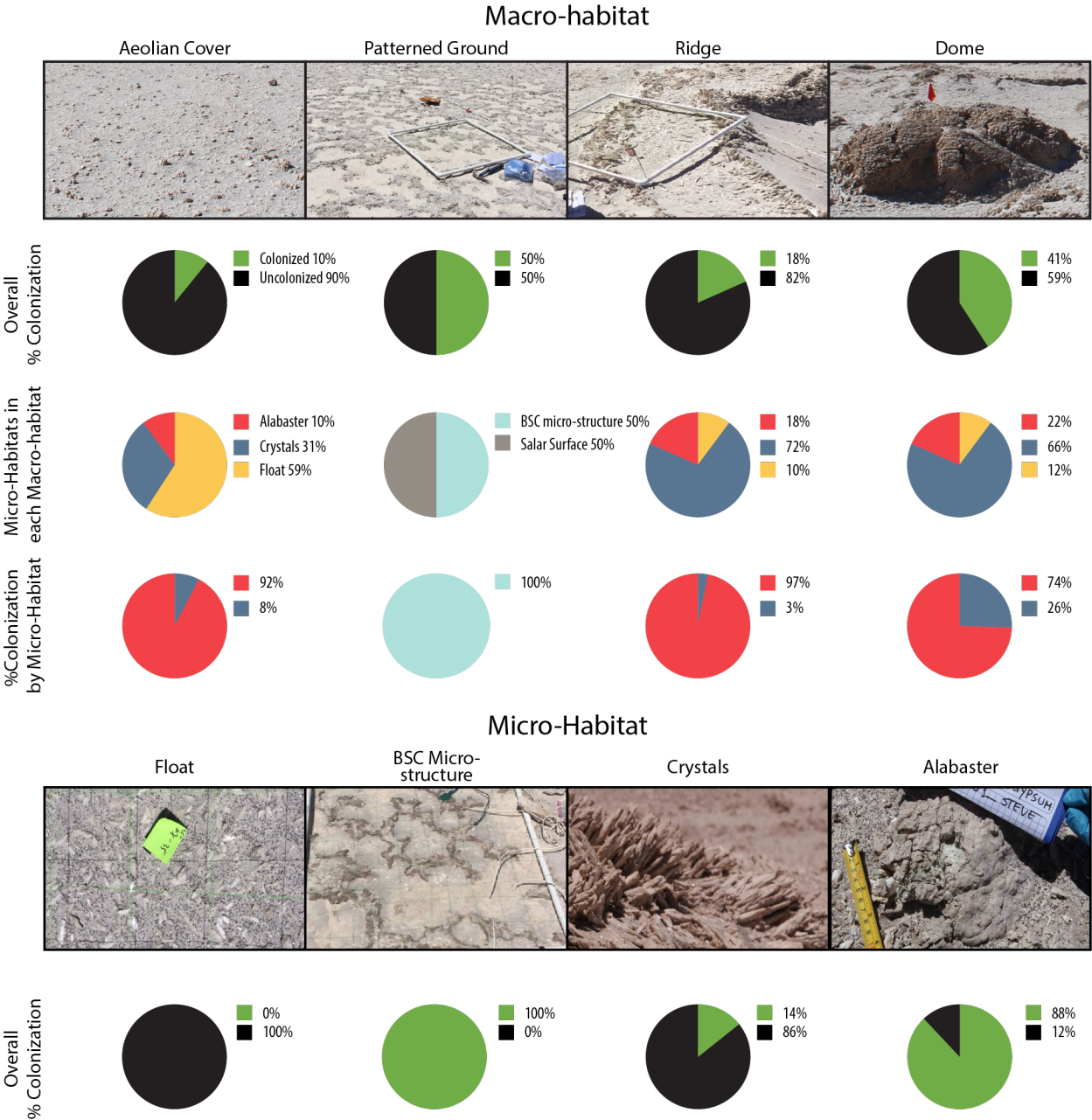


Fig. 3. Macro and Microhabitat Composition and Biosignature Detection Probabilities. Columns are by habitat and rows by indicator. For example, 90% of aeolian cover macrohabitat samples were uncolonized, while 10% had photosynthetic community biosignatures. In the aeolian cover macrohabitat, 59% of samples were float (0% of float samples were colonized, i.e. no samples contained biosignatures), 10% were alabaster (92%Col) and 31% were crystals (8%Col). By microhabitat, 0% of all float samples had biosignatures. Probabilities, standard errors and methods are further detailed in Methods, Extended and Supplementary Data sections.

Variation in %Col between microhabitats (i.e., substrate materials) was more variable than that between macrohabitats (Table 1, Extended Data Table 2). Alabaster microhabitats were almost

universally inhabited and were the most reliable predictor of biosignatures (Fig. 3, Table 1, Extended Data Fig. 3, Extended Data Table 2; Supplementary Tables 1-2). Float and sand were rarely colonized, except when sand was near alabaster (Supplementary Table 2, Supplementary Fig. 4). Crystal colonization was macrohabitat-dependent and ranged from <5% in aeolian cover to 33% in domes. Fine-scale mapping (Extended Data Fig. 2) identified two types of crystals (Type I or Type II). Type II crystals are distinguishable by a powdery alabaster layer topping the crystal, and this textural difference was significantly correlated with higher biosignature probabilities (Extended Data, Fine-scale statistical analyses). Alabaster was thus strongly associated with the presence of biosignatures regardless of macrohabitat. Patterned ground colonization was binary: all microstructures supported photosynthetic communities, whereas all bare salar surface samples contained no biosignatures (Fig. 3, Table 1).

Water Availability is the Dominant Control on Habitability and Spatial Patterns at All Scales

We hypothesized that macro and microhabitats are proxies for water availability at Pajonales and the underlying spatial heterogeneity of water content acts as the primary driver for non-random habitat (e.g., alabaster) and biosignature distributions. To confirm this hypothesis, we completed *in situ* microclimate monitoring and wetting experiments (Extended Data Table 3). These data showed that alabaster, Type II crystals and microstructures capture and/or retain liquid water up to two times longer than other microhabitats. Type II crystals are often located near open cracks in domes, where efflorescence and infiltration are greatest³³. Our data revealed a significantly higher probability of endolithic biosignatures in these microhabitats (Extended Data, Fine-scale statistical analyses). Likewise, alabaster typically encompasses the bases of ridges and domes, where humidity is high. Alabaster and Type II crystals contain a well-connected 3D network of small pores (average size <6 μm ; Extended Data Fig. 4) that are absent in other microhabitats. The porous network transports brines upwards (i.e. efflorescence), explaining the higher water availability and presence of biosignatures.

Other environmental factors, such as light and nutrient content, were not predominant controls on microbial distributions at Pajonales based on microclimate data, fine-scale studies or laboratory analyses (See Extended Data, Water Availability and Controls). Nonetheless, it is important to reiterate these factors shape endolithic and BSC spatial distributions, with their effects well-documented for many hypersaline and desert environments^{1,2,4,23,34-39}.

Predictability: Habitability and Biosignature Probability Maps

To predict biosignature distributions in Pajonales we first compiled field-based data to extract scalable rules, statistical probabilities and quantitative correlations (Fig. 4). These data were used to train convolutional neural networks (CNNs)⁴⁰ and spatial generalized additive models (GAMs) to predict macro and microhabitat types, i.e. biosignature-bearing geologic materials (Fig. 5).

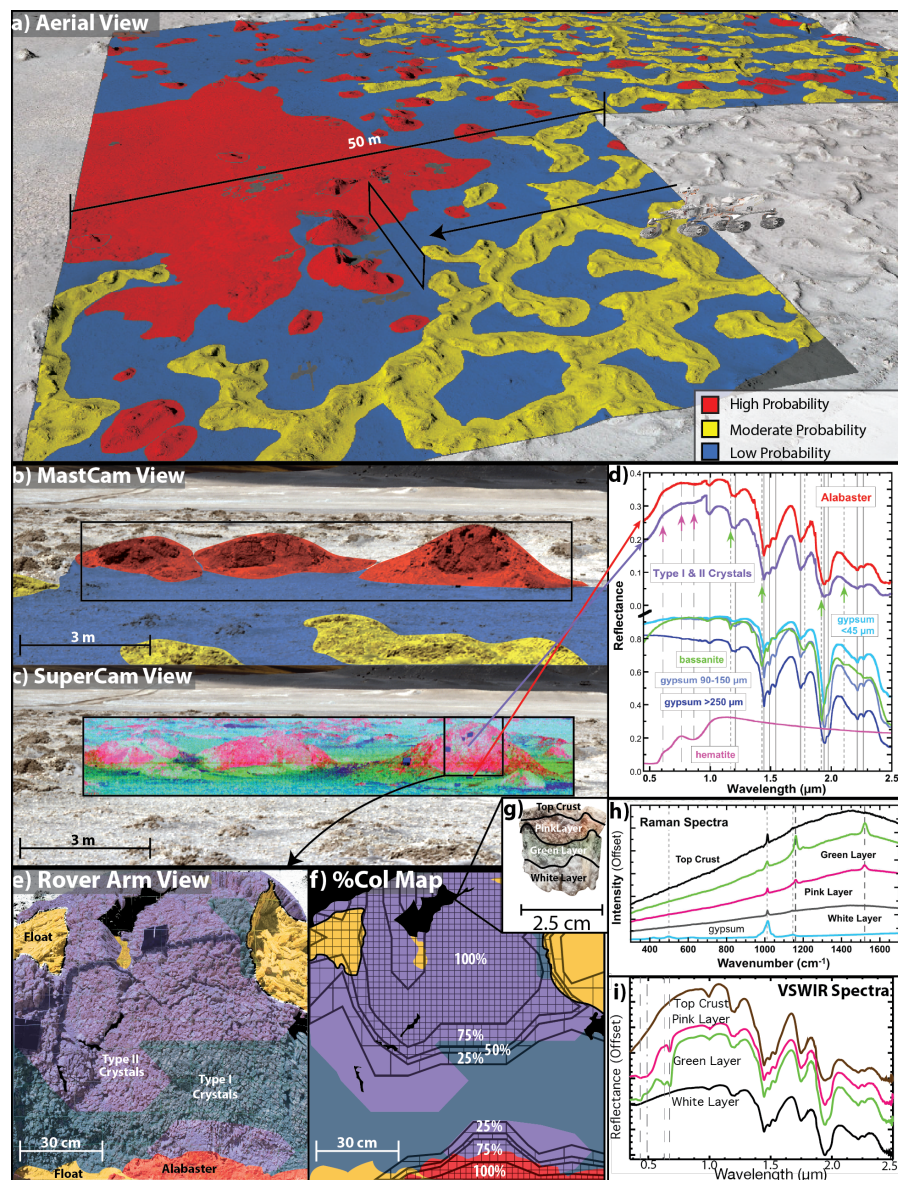


Fig. 4. Nested spatial scale biosignature probability and habitat maps. **a**, aerial-scale biosignature probability map by macrohabitat (Table 1, Extended Data Table 2); **b**, rover ground view (“MastCam”) of macrohabitat biosignature probability map; **c**, rover ground view (“SuperCam”) showing HySpex Mjölnir-acquired spectral map generated with the first three eigenimages of the minimum noise fraction transform of the hyperspectral image cube in the R, G, B channels (see Methods). In general, pink/white: Dome Type I and II crystals; green: Alabaster; **d**, HySpex Mjölnir VSWIR spectra of Dome Type I and II crystals (purple spectrum) and alabaster (red spectrum). Lab spectra of gypsum (3 grain sizes), bassanite $\text{CaSO}_4 \cdot 0.5\text{H}_2\text{O}$ (USGS spectral library), and $<125 \mu\text{m}$ hematite (Fe_2O_3)⁴¹ are plotted for reference with notable mineral absorption features indicated with vertical lines; **e**, rover arm scale microhabitat map,

based on ecological survey data (red: alabaster, yellow: float, blue-grey: Type I crystals and purple: Type II crystals); **f**, contour map of endolithic biosignatures (probability, 0-100%Col) overlain on microhabitat map of the dome shown in **e**; **g**, image of biosignatures in a Type II crystal from dome (comparable to Remote Micro Imager) showing brown/tan surface crust (top crust), pink and green endolithic biosignature layers, and a bottom white gypsum; **h**, Raman spectra (comparable to RLS on ExoMars) for Type II crystals with a strong gypsum ν_1 peak at 1013 cm^{-1} and weak peaks at 499 cm^{-1} for ν_2 and 1143 cm^{-1} for ν_3 ⁴², including colonized pink and green layers with Raman peaks at 1162 and 1523 cm^{-1} indicative of carotenoids⁴³; **i**, ASD VSWIR spectra (comparable to Mars 2020 SuperCam VISIR spectra) of Type II crystals, indicating gypsum mineralogy. Note absorption features characteristic of chlorophyll near 0.625 and $0.675\text{ }\mu\text{m}$ (dashed vertical lines) in the green spectrum and of chlorophyll near $0.675\text{ }\mu\text{m}$ and carotenoids near $0.5\text{ }\mu\text{m}$ (dash-dot vertical line) in the pink spectrum. These ASD data suggest the detector is at least as sensitive as the laboratory cell counts reported for the colored band layers (Supplementary Fig. 2).

CNN (Fig. 5 b, c ‘prediction’) and GAM model (Fig. 5 d) results aligned well with ground-truth data (Fig. 4; ‘true’ in Fig. 5 b, c). At the aerial scale (Extended Data Table 1), the influences of physical and hydrological processes were evident amongst macrohabitats, each with distinct biosignature detection probabilities (Figs. 4-5 a, Table 1, Extended Data Tables 2,4). At UAV and HiRISE spatial resolutions (Fig. 5a), a fully-connected CNN model classified, on a per-pixel basis, the four main types of macrohabitats across Pajonales. Identification confidence values ranged between 78.8% and 95.1% (UAV, aerial scale) and 54.8% and 87.0% (HiRISE, orbital scale).

At ground to fine (m-to-cm) scales, CNN and GAM model results reflected ecological statistical results (Figs. 4-5) and confirmed that microhabitat type is a credible and diagnostic predictor for the presence of biosignatures. GAM models identified alabaster as the most effective (positive) predictor for biosignatures regardless of macrohabitat (Figs. 4f, 5d). These models also flagged float and sand as having the weakest associations (negative predictors, Supplementary Tables 3-4). CNN models were trained on images of geological materials (e.g., alabaster, Type II crystal) within dome and aeolian cover macrohabitats and performed well on validation and test datasets (i.e. images withheld during network training, Fig. 5 b, c and Supplementary Figs. 5-8). For instance, alabaster was predicted with a median accuracy of 76% and a range of 65 - 90% across 10 runs with random train/validation/test partitions (or ‘splits,’ see Methods for accuracy definition and details on model runs, Supplementary Fig. 6). Thus, CNN models demonstrated predictive capability for the presence of geological materials with high probability for containing biosignatures.

Together, the empirical conditional probabilities and spatial biosignature distributions quantified above are representative of Pajonales as a whole. However, as with any statistical model, further honing of the CNN and GAM models to capture other effects will require more training data. Future work on terrestrial-trained CNN networks will expand model capabilities to include

249 physical scale of the features of interest and instrumentation. In addition to CNNs, generative
250 models (e.g., cellular automata simulations) could explore interactions between life and its physi-
251 cal environment. 44

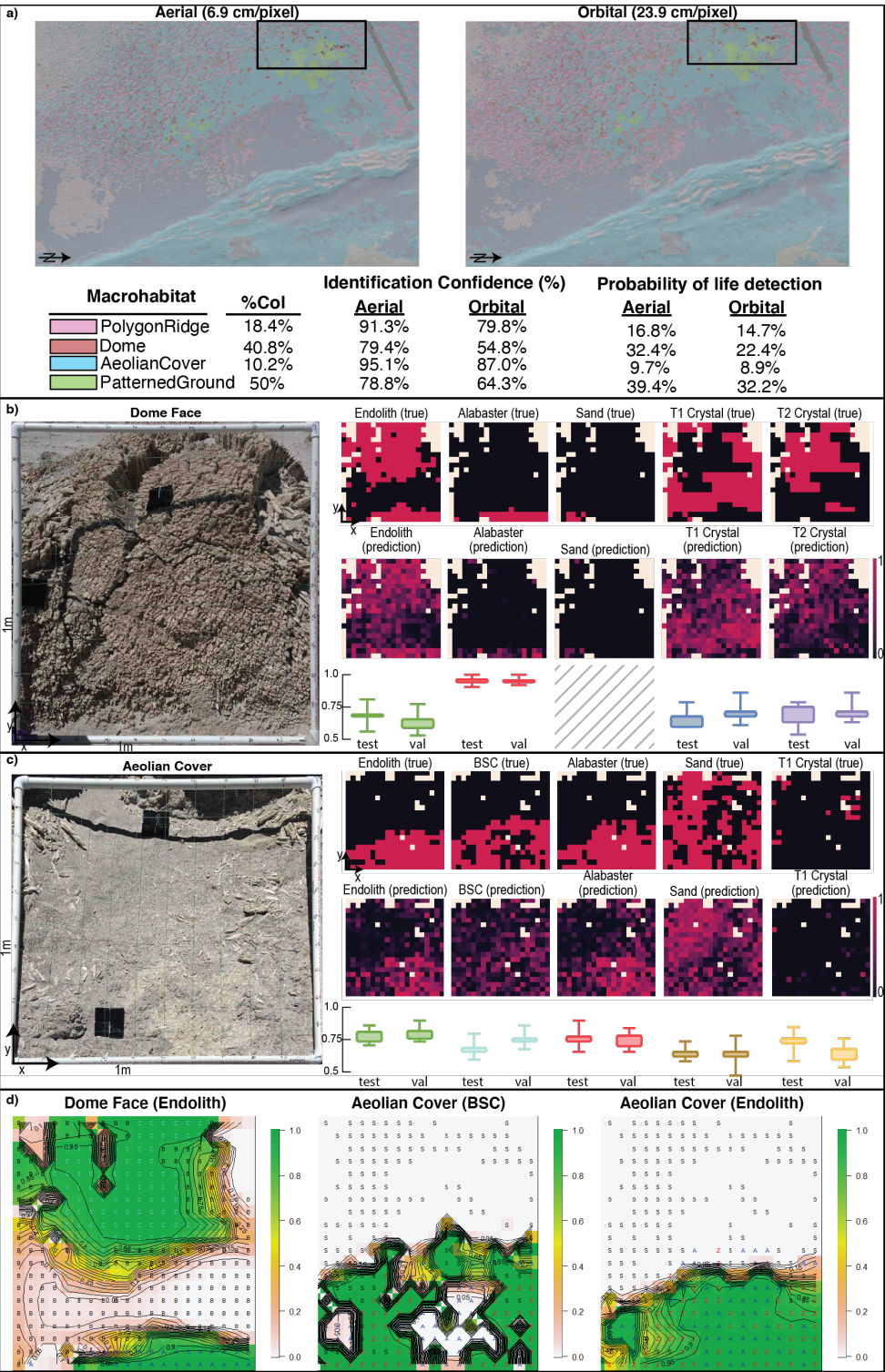


Fig. 5. Habitat and biosignature probability maps from convolutional neural network (CNN) and spatial generalized additive models (GAM). **a (top)**, Pixel-wise classification of images with ground sampling distances of 6.9 cm/pixel (Aerial) and 23.9 cm/pixel (Orbital), generated by a fully connected CNN (details in Methods). **a (bottom)**, Colors corresponding to macrohabitats in classification scenes (top), and probability of biosignatures, CNN identification confidence values, and biosignature detection expected values (identification confidence x %Col); **b**, Dome macrohabitat fine-scale (cm) CNN results for classification at the grid-cell image level; **b (top row)** “true” shows Study ES-3 ground-truth data; **b (middle row)** CNN “predictions” for presence of endolithic biosignatures and microhabitat type. Note predictive heatmaps represent CNN predictive capability over the macrohabitat images (split into training/validation/test sets) and belong to just one of the 10 randomized runs, each with a random training/validation/test split [see methods for randomized run definition and Supplementary Fig. 6 for recall/precision curve per randomized split]; **b (bottom row)** Classification accuracy (y-axis) across 10 randomized runs, summarized by box-plots; **c**, Aeolian cover macrohabitat CNN results. **c (top row)** “true” shows ground-truth data and **c (middle row)** shows CNN “predictions”; **c (bottom row)** Classification accuracy (y-axis) across 10 randomized runs; **d (left)** GAM contour map of probability of endolithic biosignatures in dome (see Methods and Supplementary Tables 3-4 for model details including parameter estimates and odds ratios). A = alabaster, B = Type I crystal, and C = Type II crystal. Note biosignature-bearing ‘transition zones’ (tz) at boundary of Type I and Type II crystals or alabaster; **d (center)** GAM probability contour map of BSC biosignatures in aeolian cover. A = alabaster, S = sand, Z = alabaster+sand; **d (right)** GAM contour probability map of endolithic biosignatures in aeolian cover (Supplementary Tables 3-4). Note probabilities of biosignatures in sand in upper half are zero, whereas sand (orange, yellow and pink colors) with alabaster (green color) in transition zones is colonized. Color ramp: red (probability = 0) to green (probability = 1).

Application as a Guide and Future Direction in the Search for Biosignatures on Mars

The framework and models presented here demonstrate how quantitative systems ecology melded with deep-learning feature recognition and prospecting can be a powerful tool to expedite the search and detection of biosignatures in terrestrial analogs. For the Pajonales test site, the pairing of empirical biosignature probabilities with AI/ML models enhanced success through identification and prediction of macro and microscopic biosignature-bearing targets. Whereas a random search yielded a 9.2% probability of detecting biosignatures, the targeted search of macro and microscale geologic features and materials, guided by machine learning models, delivered up to an ~87.5% chance of locating biosignatures in the first sample while reducing the initial search space by 85-97%. In light of these advances, our new approach represents a path forward for terrestrial analog research to produce scientific results that are objective, comparable and replicable, as well as novel in codifying expert experience.

Terrestrial analogs are foundational to successful exploration on Mars^{16-19, 30-31,45-48}. Our study provides a clear and defined general path (at different scales) for astrobiological exploration, focused on Mars and tested and applied, as a whole, at a specific analog site. The sulfate-chloride paleolake system at Pajonales arises from evaporation over millennia in a climate that may be one of the best available Earth analogs to the Noachian/Hesperian transition on Mars²⁰. The macro and microscopic structures and biotic systems modeled in this study represent an important addition to

the catalog of terrestrial Mars analogs in the literature ^{1,4,16,30,31,38} (Extended Data Fig. 1) and the only one to date with quantitative probabilities for biosignatures.

Our study generated predictive models (Fig. 5) and exploration roadmaps (Fig. 4, Example roadmap, Extended Data) for extant biosignatures within a polyextreme environment. AI/ML models successfully learned to identify macro and micro geologic features with the highest probability of containing biosignatures. This first, proof of concept deep-learning-based feature recognition ⁴⁹ for predictive biosignature exploration in a specific analog relevant to Mars exploration was selected to highlight and test the fundamentals of this method within logistical and budgetary constraints. However, the method is not limited to this analog and we encourage the astrobiology community interested in Mars exploration and life in extreme environments to consider our approach for standardizing research across terrestrial analog sites, features, instrument suites, and (bio)signatures. Spectral analyses on Mars rely on libraries of reference spectra first compiled in controlled settings on Earth⁵⁰; similarly, the interpretation of martian environments could be advanced through a library of quantitative reference information on biosignature distribution and ecological data from a multitude of Earth-based analogs compiled with a coherent methodological framework. Such a library could assist future Mars mission scientists in the selection of facies, mineral assemblages, and structures with the highest chance of containing biosignatures. Ultimately, we hope the approach will facilitate compilation of a databank of biosignature probability¹³ and habitability algorithms, roadmaps and models and serve as a guide for exploration on Mars. The framework may also have applications to other astrobiology targets including the surface of Titan or ice cover of Europa.

Correspondence and requests for materials should be addressed to K Warren-Rhodes (krhodes@seti.org).

Acknowledgments. This study was supported by the NASA Astrobiology Institute (NAI) via Grant No. NNA15BB01A. KWR dedicates this paper to her mentors Professors F. Bash, W. Jefferys, and M. Oakes and N. Fowler at the UT Austin Dept. Astrophysics and Dept of Ecology, Profs. M. Foster and J. Harvey, Statistical Ecology, Moss Landing Marine Laboratory, and to Dr. CP McKay at NASA Ames Research Center. The authors gratefully acknowledge XRD data and its respective

analysis generated from the MAINI's scientific equipment and Centro de Biotecnología at Universidad Católica del Norte. GCD and CD thank BHP Minerals Americas Project 32002137 (2016-2020). The authors thank K. Phillips (kennydphillips.com) for graphic design. VP thanks Spain Ministry of Science and Innovation grants no. RTI2018-094368-B-I00 and MDM-2017-0737 for funding and Miriam García-Villadangos for technical support.

Author Contributions. KWR, MP, NH, NC, KLR designed and implemented the experiment. KWR, MP, CTC, KLR, NC, NH, VP, PS, PS, CJ, CR, CD conducted field operations and sampling. JM, MP, CM, PS, PS, DW collected *in situ* visible, multi- and hyperspectral data from instruments and instrumented drones. MP, FK, DA, AC, LBN, KL and KWR developed deep learning and statistical models. KWR, MP, KLR, VP, NH, JLB processed samples and conducted geochemical and mineralogical analyses. KWR, MP, KLR, CTC, NH, CD, GCH, MH, VP, MM performed geological and biological analyses. KWR, KR, DW, GCH, DA, CTC installed, collected and analyzed microclimate data. All authors wrote the manuscript. NC conceived the NAI project study. KWR, KLR and NH designed the ecological study. All authors reviewed and edited a manuscript draft.

Reference List

- Des Marais, DJ. The biogeochemistry of hypersaline microbial mats. *Advances Microbial Ecology*, **14**, 251-274 (1995).
- Belnap, J. Welter, J., Grimm, N., Barger, N. & Ludwig, J. Linkages between microbial and hydrologic processes in arid and semiarid watersheds. *Ecology* **86**(2), 298-307 (2005).
- Houghton, J., Fike, D., Druschel, G., Orpha, V., Hoehler, T. & DJ Des Marais. Spatial variability in photosynthetic and heterotrophic activity drives locale $\delta^{13}\text{C}_{\text{org}}$ fluctuations and carbonate precipitation in hypersaline microbial mats. *Geobiology*, **12**, 557-574 (2014).
- Allwood, A., Walter, M., Burch, I. & B. Kamber. 3.43 billion-year-old stromatolite reef from the Pilbara Craton of Western Australia: Ecosystem-scale insights to early life on Earth. *Precambrian Research*, **158**, 198-227 (2007).
- Al-Najjar, M., Ramette, A., K hl, M., Hamza, W., Klatt, J. & L. Polerecky. Spatial patterns and links between microbial community composition and function in cyanobacterial mats. *Frontiers in Microbiology*, **5**, 406, 1-11 (2014). Doi:10.3389/fmicb.2014.00406.
- Warren-Rhodes, K., Dungan, J., Piatek, J. & McKay, C. Ecology and spatial pattern of cyanobacterial island patches in the Atacama Desert. *JGR Biogeosciences* **112**, G04S15, doi:10.29/206JG000305 (2007).
- Allwood, A., Walter, M., Kamber, B., Marshall, C. & I. Burch. Stromatolite reef from the early Archaean era of Australia. *Nature*, **441**, 714-718 (2006). Doi:10.1038/nature04764.
- Meslier, V., Casero, M., Dailey, M., Wierzbos, J., Ascascio, C., Artieda, O., McCullough, P. & DiRuggiero, J. Fundamental drivers for endolithic microbial community assemblies in the hyperarid Atacama Desert. *Environmental Microbiology*, **20**(5), 1765-1781 (2018). Doi:10.1111/1462-2920.14106.

9. Finstad, K., Probst, A., Thomas, B., Anderson, G., Demergasso, C., Echeverria, A., Amundson, R. & Banfield, J. Microbial Community Structure and the Persistence of Cyanobacterial Populations in Salt Crusts of the Hyperarid Atacama Desert from Genome-Resolved Metagenomics. *Frontiers in Microbiology* **8**, 1435. doi: 10.3389/fmicb.2017.01435 (2017).
10. Wilhelm, M., Davila, A., Parenteau, M., Jahnke, L., Abate, M., Cooper, G., Taylor Kelly, E., Parro García, V., Villadangos, M., Blanco, Y., Glass, B., Wray, J., Eigenbrode, J., Summons, R. and K. Warren-Rhode. Constraints on the metabolic activity of microorganisms in Atacama surface soils inferred from refractory biomarkers: Implications for Martian habitability and biomarker detection. *Astrobiology*, **18**, 955-966. doi: 10.1089/ast.2017.1705 (2018).
11. Dillon, J., Miller, S., Bebout, B., Hullar, M., Pinel, N. & D. Stahl. Spatial and temporal variability in a stratified microbial mat community. *FEMS Microbiology Ecology*, **68**, 46-58 (2009).
12. Rillig, M. & J. Antonovics. Microbial biospherics: The experimental study of ecosystem function and evolution. *PNAS*, **116**, 11093-11098 (2019). Doi:10.1073/pnas.1904326116.
13. Sephton, M., & Carter, J. The chances of detecting life on Mars. *Planetary Space Science* **112**, 15-22 (2015).
14. Naveh, Z., & Lieberman, A. S. Landscape ecology: theory and application. Springer Science & Business Media. (2013).
15. Mony, C., Vandenkoornhuyse, P., Bohannan, B. J.M., Peay K. & Leibold, M. A. A landscape of opportunities for microbial ecology research. *Frontiers Microbiology* **11**, 2964, doi:10.3389/fmicb.2020.561427 (2020).
16. Summons, R. *et al.*, Preservation of Martian organic and environmental records: Final report of the Mars biosignature working Group. *Astrobiology*, **11**, 157-181 (2011).
17. Farmer, J. & DJ Des Marais. Exploring for a record of ancient Martian life. *Journal Geophysical Research* **104** (E11), 26,977-26,995 (1999).
18. Stoker *et al.*, We should search for extant life on Mars in this decade, BAAS, Vol 53, Issue 4, Planetary/Astrobiology Decadal Survey 2023-2032, Whitepapers #112.
19. Jakowsky, B. Byrne, S., Calvin, W., Curry, S., Ehlmann, B., Eigenbrode, J., Hoehler, T., Horgon, B. *et al.* Mars, the Nearest Habitable World—A Comprehensive Program for Future Mars Exploration, BAAS, Vol. 53, Planetary/Astrobiology Decadal Survey 2023-2032, Whitepapers #112.
20. Hinman, N. *et al.* Surface morphologies in a Mars analog Ca-sulfate Salar, High Andes, Northern Chile. *Frontiers Astronomy Space Science*, doi:10.3389/fspas.2021.797591 (2022).
21. Cabrol, N., Feister, U., Häder, D. P., Piazena, H., Grin, E. & Klein, A. Record solar UV irradiance in the tropical Andes. *Frontiers Environmental Science* **2**, 1-19, doi:10.3389/fenvs.2014.00019 (2014).
22. Flahaut, J., Martinot, M., Bishop, J. L., Davies, G. R. & Potts, N. J. Remote sensing and in situ mineralogic survey of the Chilean salars: An analog to Mars evaporate deposits? *Icarus* **282**, 152-173 (2017).
23. Wierzchos, J., DiRuggiero, J., Vitek, P., Artieda, O., Souza-Egipsy, V., Skaloud, P., Tisza, M., Davila, A., Vilchez, C., Garbayo, I., & C. Ascaso. Adaptation strategies of endolithic chlorophototrophs to survive the hyperarid and extreme solar radiation environment of the Atacama Desert. *Frontiers Microbiology* **6**(934), 1-17 (2015)
24. Lynch, K., Horgon, B., Munakata-Marr, J., Hanley, J., Schneider, R., Rey, K., Spear, J., Jackson, A. & Ritter, S. Near-infrared spectroscopy of lacustrine sediments in the Great Salt Lake Desert:

- An analog study for Martian paleolake basins. *J. Geophysical Research Planets*, **120**, 599-623, doi:10.11002/2014.JE004707 (2015).
25. El-Maarry, M., Pommerol, A. & Thomas, N. Analysis of polygonal cracking patterns in chloride-bearing terrains of Mars: Indicators of ancient playa settings. *Journal of Geophysical Research* **113**, 2263-2278, doi:10.1002/2013JE004463 (2013).
 26. Onstott, T. *et al.* Paleo-rock-hosted life on Earth and the search on Mars: A review and strategy for exploration. *Astrobiology* **19**, 1230-1262, doi:10.1089/ast.2018.1960 (2019).
 27. Davila A. & Schulze-Makuch, D. The Last Possible Outposts for Life on Mars. *Astrobiology* **16**, 159–68 (2016).
 28. Osterloo, M. M. *et al.* Geologic context of proposed chloride-bearing materials on Mars. *Journal Geophysical Research* **115** (E10), 1–29 (2010).
 29. Rapin, W. *et al.* An interval of high salinity in ancient Gale crater lake on Mars. *Nature Geoscience* **12**, 889-895, doi:10.1038/s41561-019-0458-8 (2017).
 30. Bosak, T., Moore, K., Gong, J. & Grotzinger, J. Searching for biosignatures in sedimentary rocks from early Earth and Mars. *Nature Reviews Earth and Environment* **2**, 490-506 (2021).
 31. Balci, N., Gunes, Y., Kaiser, J., On, S., Eris, K., Garczynski, B., & Horgan, B. Biotic and abiotic imprints on Mg-rich stromatolites: Lessons from Lake Salda, SW Turkey. *Geomicrobiology Journal* **37**, 401-425, doi:10.1080/01490451.2019.1710784 (2020).
 32. Williams, A., Buck, B., Soukup, D. & Merkler, D. Geomorphic controls on biological soil crust distribution: A conceptual model from the Mojave Desert (USA). *Geomorphology* **195**, 99-109, doi:10.1016/j.geomorph.2013.04.031 (2013).
 33. Warren, J. *Evaporites: A Geological Compendium, Second Edition*. Springer: Berlin, 1829 pp. (2016).
 34. Wierzchos, J. *et al.* Microbial colonization of Ca-sulfate crusts in the hyperarid core of the Atacama Desert: implications for the search for life on Mars. *Geobiology* **9**, 44-60, doi:10.1111/j.1472-4669.2010.00254.x (2010).
 35. Robinson, C. K., Wierzchos, J., Black, C., Crits-Christoph, A., Ma, B., Ravel, J., Ascaso, C., Artieda, O., Valea, S., Roldán, M., Gómez-Silva, B., & Diruggiero, J. (2013). Microbial diversity and the presence of algae in halite endolithic communities are correlated to atmospheric moisture in the hyper-arid zone of the Atacama Desert. *Environ. Microbiol.*, **17**(2): 299–315.
 36. Jørgesen, B. & Des Marais, D. Optical properties of benthic photosynthetic communities: Fiber-optic studies of cyanobacterial mats. *Limnology Oceanography* **33**, 99-113 (1988).
 37. Szyrkiewicz, A., Moore, C., Glamoclija, M., Bustos, D. & Pratt, L. Origin of coarsely crystalline gypsum domes in a saline playa environment at the White Sands National Monument, New Mexico. *Journal Geophysical Research* **115**, F02021, doi:10.1029/2009JF001592 (2010).
 38. Walker, J., Spear, J. & Pace, N. Geobiology of a microbial endolithic community in the Yellowstone geothermal environment. *Nature* **434**, 1011-1013 (2005).
 39. Rasuk, M. *et al.* Microbial characterization of microbial ecosystems associated to evaporites domes of gypsum in Salar de Llamara in Atacama Desert. *Microbial Ecology* **68**, 483-494 (2014).
 40. Chen, L., Papandreou, G., Kokkinos, I., Murphy, K. & Yuille, A.. Semantic Image Segmentation with Deep Convolutional Nets and Fully Connected CRFs. *CoRR*, abs/1412.7062 (2015).

41. Bishop, J. L. & Murad, E. in *Volcano-Ice Interactions on Earth and Mars*. J. L. Smellie & M. G. Chapman (eds.), p. 357-370, Geological Society, Special Publication No. 202 (2002).
42. Buzgar, N., Buzatu, A., & I.V. Sanislav. The Raman study of certain sulfates. *Analele Stiintifice ale Universitatii, Al. I. Cuza IASI Geologie. Tomul LV 1* (2009).
43. Jehlicka, J., Edwards, H. & Oren, A. Raman spectroscopy of microbial pigments. *Appl Environ Microbiol*, **80**, 3286-3295. Doi:10.1128/AEM.00699-14.
44. National Academies of Sciences, Engineering & Medicine. *Origins, Worlds and Life: A Decadal Strategy for Planetary Science and Astrobiology 2023-2032*. The National Academies Press (2022). doi:10.17226/26522.
45. Farmer, J. Habitability as a Tool in Astrobiological Exploration. Ch. 1 in *From Habitability to Life on Mars*, pp. 1-12. Elsevier (2018).
46. Hays, L. *et al.* Biosignature preservation and detection in Mars analog environments. *Astrobiology* **17**, 363-400 (2017).
47. Fairen, A. *et al.* Astrobiology through the ages of Mars: the study of terrestrial analogues to understand the habitability of Mars. *Astrobiology* **10**, 821 (2010).
48. Green, J., Hoehler, T., Neveu, M., Domagal-Goldman, S., Scalice, D. & M. Voytek. Call for a framework for reporting evidence for life beyond Earth. *Nature* **598**, 575-579 (2021).
49. He, K., Xiangyu, Z., Shaoqing, R. & Jian, S. Delving Deep into Rectifiers: Surpassing Human-Level Performance on ImageNet Classification. *IEEE*, 1026-1034 (2015).
50. Adams, J.B., and Filice, A.L. Spectral reflectance 0.4 to 2.0 microns of silicate rock powders: *Journal of Geophysical Research*, v. 72, doi:[10.1029/JZ072i022p05705](https://doi.org/10.1029/JZ072i022p05705) (1967).

Methods

Study Location

The ~3 km² field study location (S 25.14149, W 68.77215) is situated in the eastern-central portion of the 104 km² Salar de Pajonales (Pajonales) basin, a 4.09 million year old lakebed with active lagoons and fossil salar structures (Fig. 1)^{51,52,53}. There, low precipitation (80-150 mm yr⁻¹) and high evaporation potential (1,350 mm yr⁻¹) are typical of the arid conditions of the Atacama Desert and Altiplano, and have strengthened since the Miocene⁵⁴. Average air temperature is 5°C, with values recorded as low as -20°C. Seasonal precipitation largely occurs via austral summer rains from the east (Altiplanic winter), and southerly winter storms and occasional snow. Despite significant annual precipitation, high winds, low humidity, and strong insolation combine to keep Pajonales mostly ice-free, with water availability remaining low in much of its surface environment. The water table is shallow in portions of the salar, where at least 14 perennial lagoons exist. The bedrock underlying and adjacent to the salar is associated with Cenozoic volcanism, still active today, including nearby thermal springs. Volcanic rocks are mainly of intermediate to felsic composition (andesites and rhyolites). Carbonates (calcite), borates (ulexites), chlorides (halite), quartz and minor feldspars and other minerals, locally abundant and associated with gypsum, compose the main mineral assemblage^{51,52,53}.

Physical Environment and Habitats

UAV Mapping of Habitats/Geomorphology/DEM

Our study defines a habitat as the physical environment in which a particular organism or community of organisms may live. Macrohabitats were classified first based on field observations and UAV images and subsequently refined and ground-truthed with field assessments. Initial UAV imagery and ground-based assessments revealed several surficial geomorphologic features with potential habitability, i.e., ecological macrohabitat types. These macrohabitat (Table 1) features included 1) ridge networks^{20,33} (~1 to 100 m length); 2) domes ($\leq 1\text{--}7.5$ m diameter; *tumuli*)^{20,33}; 3) fractal-like patterned ground (cm to 100s m area), comprised of bare gypsum salar surface ('salt pan') covered by microstructures (1-3 cm height)^{20,55}; and 4) aeolian surface cover ('gypsum regolith')^{20,33} between and around these features (cm-to-100s m area). These four distinct geomorphic units were mapped in ESRI ArcGIS software using an orthophoto mosaic and digital elevation model (DEM), both derived from UAV images with the software package Pix4D. Ridges were identified as elongate, continuous, positive topographic features with length:width ratio (L:W) values $>2:1$. Domes were identified as circular to subcircular, isolated, positive topographic features with L:W values $<2:1$. Patterned ground was distinguished from other flat surfaces based on its tan color and distinct polygonal pattern. All other flat surfaces comprised aeolian cover, identified from its sandy texture, beige-grey coloration, and occasional dark and light rippling on the leeward sides of ridges and domes. A fully convolutional neural network [Deeplab V3+ model⁴² with a ResNet50 backbone⁴⁹] was trained to classify, on a per-pixel basis (i.e., semantic segmentation), the terrain in the orthophoto mosaic of the field site and surrounding area at UAV and HiRISE ground sampling distances (6.9 cm/pixel and 23.9 cm/pixel respectively). Training images were labeled by a human analyst with on-the-ground experience at the field site using the criteria delineated above for ridges, domes, patterned ground, and aeolian cover. Additional categories were added as necessary to incorporate terrain not found within the confines of the study site. Network training was carried out until the loss rate stabilized, typically <40 epochs (epoch = one complete pass of training data through the network) with final test accuracies (identification confidence) presented in Fig. 5a for each class. See also "convolutional neural networks methods" section below for details on training, validation and testing datasets.

Microhabitat (Fig. 3, Table 1, Supplementary Fig. 1) categories were identified and refined during nested spatial scale studies (described below) by visual assessments of texture, coherence and color in the field and spectral imagery acquired on the ground. We collected hyperspectral panoramic images of the dome habitat using a Hypspx Mjolnir Hyperspectral Camera mounted on a scanning tripod and placed approximately 30 m from the dome target. From each scan the pushbroom-style dual camera collects spectral data across the visual-near infrared (VNIR) to short-wave infrared (SWIR) spectral range of 400 to 3500 nm at a bandwidth sampling interval of 3.0 or 5.1 nm as it scans horizontally across the scene at a constant pan rate. We then collected three scans under clear skies in mid-afternoon lighting conditions, while calibrating the frame period and integration time of the Hypspx camera to the lighting conditions in order to maximize reflectance and eliminate saturated pixels. We then collected a final complete panoramic scan using the calibrated parameters. The final scan produced a hyperspectral image cube with a spatial resolution of ~ 0.5 cm/pixel in the VNIR spectral region and ~ 1.0 cm/pixel in the SWIR spectral region. The spectral image covers a panoramic view of the primary dome target, three smaller domes next to it, and foreground primarily composed of aeolian cover.

Raw data values in the hyperspectral image cubes acquired from the tripod were calibrated to reflectance values using in-scene Spectralon calibration targets. Each scene consists of two spatially overlapping cubes, one in the VNIR wavelength range and the other in the SWIR. Because the optical apertures for the two subsystems that collect these cubes are slightly offset, the pixels in the two component cubes are not perfectly registered in the along-scan (horizontal) direction. Thus, extraction of reflectance spectra of the alabaster and Type I and Type II crystals units (Fig. 4d) was accomplished by manually selecting the corresponding pixels from the two component cubes by referencing features observed in both. The overwhelming majority of spectra examined contain the signature of gypsum (Fig. 4d), and only subtle spectral differences between different surfaces on and around the domes were noted. Weak shoulders and slight shifts in band position were found for the Type-I and Type-II crystals material that are consistent with the presence of bassanite⁵⁶. These are highlighted by green arrows (Fig. 4d). A weak shoulder near 0.6 μm , a reflectance maximum near 0.76 μm , and a weak minimum near 0.88 μm are attributed to hematite. These features are indicated by purple arrows and are enhanced in the alabaster-type material. To highlight this subtle spectral variability and reveal any spatial patterns present in that variability, we processed the VNIR and SWIR cubes separately using the Minimum Noise Fraction Transform (MNF) principal component analysis algorithm⁵⁷. The false color image shown in Fig. 4c was created by loading the first three bands representing most significant spectral variance from the MNF-processed SWIR cube for that scene into the red, green, and blue channels of the image. The color variations in this representation correspond to slight differences in the general gypsum spectrum and are seen to be spatially segregated. While we have not undertaken a separate study to explain the causes of these spectral variations, they are likely due to differences in grain sizes, degree of compaction, and perhaps the presence or absence of different minor (non-gypsum) components.

Environmental Controls: Climate Monitoring and Wetting Experiments

Environmental data for the study location and within domes and microstructures were acquired *in situ* from Oct 2018-Nov 2019 with a HOBO® microstation (H21-001) and Onset Computers, Bourne, MA, logger array. One weather station was connected to the following smart sensors to monitor macroclimate parameters: 1) rainfall (1-mm resolution, RG3-M Hobo Rain Gauge Metric Data logger); 2) photosynthetically active radiation (PAR, S-LIA-M003), to quantify solar flux in the biologically relevant portion of the spectrum (400-700 nm; range 0 to 2700 $\mu\text{mol m}^{-2} \text{s}^{-1}$); 3) wind speed and direction (S-WCF-M003; $\pm 1.1 \text{ m s}^{-1}$, ± 7 degrees); and 4) air temperature (T, °C) and relative humidity (%RH) at 1m above dome surfaces ($\sim 3 \text{ m}$ above salar surface; HOBO® S-THB-M002; precision: $\pm 0.2^\circ\text{C}$ T, $\pm 2.5\%$ RH, shaded by a solar radiation shield, RS3-B).

Microclimate data were acquired through arrays of both stand-alone external T/RH U23 ProV2 HOBO loggers (U23-002; precision: $\pm 0.21^\circ\text{C}$, $\pm 5\%$ RH) and microstations (H21-001). To measure the presence of liquid water on surfaces and in rock interiors (endolithic microenvironments) from fog/dew/rainfall/snow, microstations were connected to 1) T/RH smart sensors (S-THB-M008); 2) leaf wetness sensors (S-LWA-M003; precision $\pm 5\%$ RH, reading of 0% RH is dry, 100% RH reflects a sensor grid completely covered by a thin layer of water); and 3) EC 5 conductivity probes (S-SMC-M005; baseline >0 : liquid water and/or 0.25 m^3/m^3 soil saturated) were placed on both the surfaces and interiors of domes at ~ 0.5 -1 cm below surface where endolithic microbial communities layers occurred. They were also placed on salar surfaces and microstructures in all four cardinal directions at ~ 0.5 -1 cm below surface where BSC layers occurred.

Based on previous studies^{58,59,60,61} and successful long-term use of RH and conductivity sensors for direct field measurement of water activity—the parameters controlling microbiological activity in hyperarid deserts^{58,59}—a cutoff for liquid water was assumed at $RH \geq 95\%$. Although lichen communities can undergo photosynthesis at 70% RH, the 95% RH threshold reflects a mid-value for the predominantly cyanobacterial endolithic communities in the dome field location, which require liquid water to initiate photosynthesis (range 90–100%)^{62–67}. For logger probes inserted into gypsum dome and microstructures, an electric drill was used to create small (~1 cm) boreholes in which T/RH sensors (S-THB-M008) were inserted and sealed with silicon epoxy. All sensors logged at 30-min intervals.

This environmental array allowed us to measure naturally available moisture sources to microbial communities, including surface precipitation (PAR- cloud/storm cover; rainfall/snow - rain gauge, leaf wetness); and concomitant available moisture of interiors of domes, microstructures and bare salar surfaces (T/RH, EC). *In-situ* rain gauge data were corroborated with nearby station precipitation data, when available, and historical climate data were obtained from reference literature, regional observatories and the Chilean Meteorological Bureau. In order to ascertain the relative role of microstructures versus bare salar surfaces in capturing and retaining water during rainfall events, a simulated rainfall wetting experiment was completed within each of three (10 mm, 1 mm and control) 1-m² quadrats. The following sensors (see above for specifications) were emplaced: 1) a leaf wetness sensor; 2) four Hobo temp/RH probes (two in microstructures at the surface and 1 cm below the surface and two in bare salar surface and at 1 cm); and 3) two EC-5 conductivity probes in microstructures at the surface and 1 cm below the surface. Sensors were placed in the field to acclimate for two days prior to the field experiment and left in field for two days post-rain. Rain events were simulated with a gentle spraying of DI water equally across the quadrat via a commercial sprayer (10 mm = 10 liter/m² and 1 mm = 1 liter/m²) at 0900 on 04/21/19. The control received no water. Visual documentation by a handheld camera was also acquired every 20 minutes during daylight for 48 hours from the application of rain events to the end of the experiment.

Mineralogy, Organic Carbon Content and Nutrient Content Analyses

The mineralogical composition of powdered specimens sieved under a mesh size of 20 μm was verified by XRD using a Bruker D8 Advance diffractometer with a graphite-monochromatic Cu K α radiation source (Cu cathode of wavelength $K\alpha=1.54051$) operated to 30 mÅ y 40 Kv. For quantitative analysis of the crystalline phases present in the samples, the Power Diffraction File (PDF-4+2016) of the International Centre for Diffraction Data (ICDD) was used.

Field Raman spectra were recorded with a customized spectrometer developed to simulate operational concepts planned for the Raman Laser Spectrometer (RLS) instrument onboard the European Space Agency's 2022 ExoMars rover mission. This field instrument performs measurements under conditions similar to those of the RLS on the ExoMars rover, including at least 20 spectra in each sample, with a 50 μm spot size at a working distance of 5 mm and an irradiance level of 0.6–1.2 kW cm² with a 532-nm continuous wave laser⁶⁸. The spectrometer covers a spectral range from 100 to 3800 cm⁻¹ with a spectral resolution of 12 cm⁻¹. The instrument was calibrated before each measurement using TECAPET®, the same calibration standard onboard ExoMars. Data products were analyzed using a statistical procedure previously applied in macro techniques, such as XRD and FT-Raman⁶⁹. Because the spot size of the instrument is only 50 μm and only single or a few grains are analyzed at a time, the statistical analysis was performed on the

relatively few (20–30) Raman spectra acquired per sample. A detailed point-by-point analysis procedure is provided in⁷⁰.

Reflectance spectrometry is useful for rapid, non-destructive, compositional identification and analysis. Phyllosilicates, carbonates, and sulfates display distinct absorption features in the short-wave infrared (SWIR) region (1–2.5 μm) and organic molecules absorb light in the visible to near infrared (VNIR, 0.4–1 μm) wavelength region^{71,72}. We used an Analytical Spectral Devices (ASD) FieldSpec 4 spectroradiometer to collect solar-illuminated VSWIR reflectance spectra of freshly exposed samples in the field under cloud-free skies and clear lighting conditions, and in the lab using a contact probe. The instrument was calibrated to a dark current and a white reference target between each measurement. Reflectance spectra are derived through subtraction of the dark current spectrum and division by the white reference spectrum. Spectra were plotted and analyzed using the Interactive Data Language Environment for Visualizing Images (IDL/ENVI) software suite. Reflectance spectra acquired with the ASD in the field are provided in Fig. 4i for four locations on a sample (Fig. 4g). These illustrate the dominant gypsum features including bands at 0.99, 1.21, 1.45–1.49–1.54 (triplet), 1.75, 1.94, 2.22–2.26 (doublet), 2.43, and 2.48 μm ⁵⁶. Two spectra acquired in the field with the HySpex Mjölnir Hyperspectral Camera are shown in Fig. 4d. The Type I and Type II crystals gypsum (purple spectrum at the top of Fig. 4d) spectrum includes shoulder features for bassanite near 1.17, 1.43, 1.92, and 2.1 μm ⁵⁶ that indicate that the Type I and Type II crystals gypsum unit is less hydrated and some of the gypsum crystals converted to bassanite. Both the alabaster and Type I and Type II crystals gypsum spectra include a shoulder near 0.61 μm , a reflectance maximum near 0.76 μm , and a weak minimum near 0.88 μm that are consistent with ferrihydrite or fine-grained hematite^{73,74}. These features are stronger in the alabaster-type spectrum, indicating that more iron oxide/oxyhydroxide is present in that sample, although the abundance is likely only a few percent in either gypsum-rich unit.

Porosity was estimated by petrographic image analysis of thin sections prepared with vertical orientation. A blue dye was injected into the epoxy to visualize porosity in the thin sections. After acquisition of the photomicrographs at 10x magnification using a Leica DM4500P LED polarizing microscope, the plane polarized light photomicrographs (Extended Data Fig. 4 a,c) were first normalized using the auto white balance function in GIMP image processing software (GIMP 2.10.18; <https://www.gimp.org/>). In a second step a selection mask with a RGB threshold of 50 was applied to select blue areas (pores) in the individual images. The selection was exported to Image J (<https://imagej.nih.gov/ij/>). In Image J, binary images (Extended Data Fig. 4 b,d) were created that subsequently were used to analyze the percent area of pixels (black pixels in images Extended Data Fig. 4 b,d) representing porosity.

Nutrient content was measured on powdered samples. Instrumentation for total carbon (TN), total organic carbon (TOC), and total nitrogen (TN) was the Exeter Analytical, Inc. (North Chelmsford, MA) CE-440 Elemental Analyzer. Inorganic carbon was removed from samples prior to measurement of TOC by acid extraction. This introduces the possibility that some organic compounds are lost during the extraction and rinsing process. Total phosphorous (TP) was extracted from powdered samples in a two-step process: combustion at 500°C followed by dissolution in 0.15M HCl. The extracts were analyzed with the Astoria Pacific (Clackamas, OR) A2 Segmented Flow Analyzer by the molybdate blue method. Accuracy and precision are a standard error range that is less than the minimum detectable limit.

Water soluble anions and low molecular weight organic acids were analyzed by Ion Chromatography (IC). Two grams of grounded samples were diluted in 10 ml of deionized water, sonicated (3 \times 1 min cycles), and filtered through a 0.22 μm pore size. The filtrate was loaded into

a Metrohm 861 Advanced compact ion chromatographer (Metrohm AG, Herisau, Switzerland). Twelve anionic species were measured simultaneously: inorganic, such as fluoride, chloride, bromide, nitrate, nitrite, sulfate, and phosphate; and five low molecular weight organic acids, such as acetate, propionate, formate, tartrate, and oxalate. A Metrosep A supp 7-250 column was used with 3.6 mM sodium carbonate (NaCO_3) as eluent.

Microbial Ecology Methods

As in most analog studies, our research began with initial observations to generate scientific hypotheses. In a second step we amassed statistical data at hierarchical scales to test these hypotheses (Figs. 2-3, Extended Data Figs. 1-2; Supplementary Fig. 1). We then quantified the probabilities for biosignatures and repeatedly tested and honed them, enabling the formation of new hypotheses, predictions and rules in an iterative cycle (Extended Data Fig. 2). The resultant robust set of quantitative biosignature, geomorphological and ecological data, rules and probabilities then formed the inputs to deep learning models to construct habitability and biosignature heat maps and models (Figs. 4-5).

Quantifying Photosynthetic Microbial Community Abundance (Probability of Colonization) and Mapping Spatial Distribution: Overall Approach

Photosynthetic microbial community colonization at Pajonales was investigated from orbit to ground scales with a multi-year, multi-disciplinary approach that tightly integrated traditional molecular and ecological methods, UAV surveys and ground-based spectroscopic and panoramic camera instruments. We completed an initial field survey, three iterative microbial landscape ecology studies, microenvironmental monitoring, and wetting experiments to quantify photosynthetic microbial colonization and identify the controls on microbial abundance and spatial pattern. The study collected presence/absence data, an approach commonly employed in ecology to reduce time and sampling effort, with data collected from e.g., specific points, grid cells, quadrats. Specifically, we quantified the abundance of photosynthetic microbial communities at multiple scales (i.e., location to micro scales) as the probability of a sample containing a biosignature, or percent microbial community colonization (%Col) which was defined as the number of samples (or macro or microhabitats) containing biosignatures \div the total number of samples (or macro or microhabitats) $\times 100^{75-90}$.

Initial Field Campaign and Assessment

The first-year field campaign (Oct 2016) was dedicated to a pilot survey of the biogeochemical, biological, ecological, mineralogical and geophysical features of the Pajonales location. Two UAV flight surveys (north location 0.237 km²; south location 0.198 km²) and three days of ‘walkabout’⁹¹ surveys were completed by the team. It was during these surveys that the first visible presence of cryptic endolithic photosynthetic microbial communities in geomorphological structures was discovered and confirmed *in-situ* by VNIR and Raman spectroscopic instruments, revealing beta-carotene and chlorophyll in the banded orange and green endolithic biosignature layered bands, respectively.

Initial Data Analysis and Landscape Study Design

Walkabout survey and UAV image data from the field campaign served as the baseline to i) define relevant scales of interest for the study (Extended Data Table 1), ii) identify and classify geomorphic features of the Pajonales landscape (see UAV mapping above and Extended Data Fig. 1), and iii) generate initial hypotheses and a detailed research design and sampling plan, which included three comprehensive microbial landscape ecology studies (2016-2019; Extended Data Fig. 2). All three studies included both UAV and ground-based components and tested hypotheses and generated results, rules and probabilities for biosignatures that served as inputs to the iterative hypothesis testing and refinements of the subsequent study (Extended Data Fig. 2). Because of the remoteness and high altitude of Salar de Pajonales, each field study was restricted to 1-2 weeks in duration based on stringent logistical, financial and safety constraints. Three ecological studies were conducted in 2018-2019 to define and map microbial colonization and allow probability functions to be quantified:

1. Ecological study (ES-1) estimated microbial abundance and patterns and the effect of spatial scale using aerial to microscale nested biosignature surveys; ES-1 i) tested initial hypotheses (Extended Data Fig. 2), ii) collected first biosignature data and refined macro and microhabitat classifications and iii) produced the first rules and biosignature probabilities. These data were then tested for predictability in ES-2.
2. ES-2 quantified microbial abundance and patterns and the influence of multiple sizes and types of habitats; the study tested and honed rules and probabilities from ES-1 and generated new rules and predictions for testing in ES-3 (Extended Data Fig. 2).
3. ES-3 mapped abundance and biosignature spatial pattern at fine (cm) scales within individual dome, aeolian cover and ridges (Extended Data Fig. 2). The study continued testing the rules, predications and probabilities from ES-2 and further refined them. The resultant data was then the basis for generating habitability and biosignature probability heatmaps, spatial analyses (Global Moran's), and deep learning models (convolutional neural network, CNN; generalized additive models, GAMs) (see deep learning sections below).

To investigate the effect of spatial scale (ES-1) on the probability for photosynthetic microbial community biosignatures (% col) the study location was subdivided into nested hierarchical scales of study, including quadrants (red grid, 50m x 50 m), areas (black grid, 5 m x 5 m), and microsites (see Extended Data Figs. 1-2). All samples in ES-1 were randomly chosen based on spatial scale (i.e., not based on habitat types). UAV imagery was initially classified as raised areas (ridges and domes) or 'flat' areas [aeolian cover (grey) and patterned ground (green)]. Initial study hypotheses were that i) %Col varied significantly by spatial scale (ES-1) and ii) that 'raised' geomorphic features (perhaps linked to preferential water availability or more suitable rock architecture for colonization)^{12,92,93,94} were more habitable than flat features, i.e., that geomorphic unit/ecological habitat type controlled colonization (ES-2). These habitat classifications were iteratively refined over the course of the project (ES-2 and ES-3) as an understanding of the features and associated microbial inhabitants evolved. Furthermore, the 'abiotic' patterned ground observed in 2016 by aerial imagery (green unit) was in 2018 ground surveys ascertained to be microstructures with living photosynthetic biological soil crust communities (BSC). To accommodate these new findings, we created microstructure and bare salar surface microhabitat and BSC biological morphotype categories and separated these data from the endolithic colonization mode analyses.

Scales of Study

Ecologically relevant scales of study (i.e., scales of microbial communities and their interactions) can range from the planetary to the nano-scale. Spatial scales of choice for a study can also be circumscribed by the particular methods selected, instruments deployed, and/or features of interest. The 2016 walkabout surveys and UAV imagery revealed surface geomorphologic units and features of varying scales with potential habitability. One initial hypothesis centered on these features as habitat units of ecological importance (e.g., ‘raised’ versus ‘flat’ units) that could influence the abundance and spatial pattern of microbial communities across the landscape, as has been documented in earlier studies^{93,94}. Extended Data Table 1 defines the nested hierarchical scales of physical features in the Pajonales location.

Proteomic and Metagenomic Studies

The methods and results for the Pajonales project’s metagenomic and proteomic investigations will be detailed in future companion papers. However, for completeness, here we provide a summary of those studies. Briefly, to identify the microbial composition of endolithic photosynthetic communities, DNA was extracted from 2 g of wet weight soil from each sample according to FastDNA SPIN kit for soil method (MPbio). We quantified the DNA and its integrity using a Nanodrop (NP1000) labeling the ratio of DNA/RNA 260/230 and the ratio of DNA/protein 260/280. In addition, microbial diversity through Miseq Illumina sequencing of hypervariable regions of 16S rRNA for Bacteria (V1-V3) were carried out using universal bacterial primer (27F/519R) 16S rRNA gene amplification with standard protocols⁹⁵. Amplicon sequencing was performed using (www.mrdnalab.com) the manufacturer’s guidelines. Multiplex fluorescent immunoassays were used for rapid estimation of the presence of microbial markers and main metabolic traits: 0.5 g of powdered samples were analyzed with the SOLID-LDChip immunosensor (*Signs of Life Detector-Life Detector Chip*^{96,97,98}, by a fluorescent sandwich microarray immunoassay^{98,99,100}. The LDChip is the core sensor of the SOLID (Signs of Life Detector) instrument for detecting possible traces of life in the field of planetary exploration^{99,101}. The LDChip used in this work contained 200 polyclonal antibodies produced against a wide range of immunogens (small organic molecules; peptides and proteins; exopolysaccharides and lipopolysaccharides; spores and whole cell lysates of bacteria and archaea, including 20 antibodies to different cyanobacterial strains^{97,99}.

Proteomic and genomic studies revealed phototrophic communities to be dominated by bacterial phyla that included *Cyanobacteria*, *Proteobacteria*, *Actinobacteria*, *Thermi*, *Bacteroidetes* and *Chloroflexi*. *Leptolyngbya*, *Gloeocapsa Cyanotheca* and *Nostoc* comprised some of the main cyanobacterial members, which are poikilohydric organisms that “equilibrate rapidly to ambient water content”¹⁰² and are dependent upon the presence of liquid water for photosynthesis and growth. LDChip revealed the presence of a diversity of microbial markers immunodetected with antibodies to several cyanobacterial strains, *Bacteroidetes* as *Salinibacter* spp., haloarchaea as *Halorubrum* sp., thermophiles as *Pyrococcus* spp., and some potential perchlorate-reducing bacteria such as *Azospira* spp., among others. LDChip also showed positive immunodetection with antibodies to proteins involved in nitrogen fixation, and even the pink-colored light-driven proton pump bacteriorhodopsin in one of the samples.

Microbial Landscape Ecology Studies of Photosynthetic Microbial Community Biosignatures: Detailed Methods⁷⁵⁻⁹⁰

ES-1 (Spatial Scale): Quantifying Abundance and Nested Scale Spatial Patterns.

Extended Data Fig. 2 and Supplementary Fig. 1 show the spatial design and hierarchical sampling for ES-1. A random sampling scheme was adopted for each nested spatial scale^{81,82,83,86} to provide an objective representation of the probability of biosignatures, as percent colonization (%Col). The data was sampled at resolutions from hundreds of m to cm. To be considered representative $\geq 10\%$ of the Pajonales study location was mapped. Two randomly selected quadrants (50 m x 50 m) were chosen. A third quadrant was added for the habitat surveys for ES-2. Within each quadrant, we randomly selected four 'areas' (5 m x 5 m), nine 'sites' (1 m x 1 m) within each area, and three 'microsites' (10 cm x 10 cm) within each site (n=216 samples).

Within each microsite, the following data was recorded: i) presence/absence of visible photosynthetic communities/biosignatures; ii) aspect/orientation of visible biosignatures (4 cardinal directions) and depth (to cm) and color of colonized layers; iii) microhabitat type(s); iv) samples for mineralogy and nutrient content; v) samples for gravimetric water content; and vi) samples for molecular biodiversity and biomarker profiling by multiplex immunoassays. Percent colonization (%Col) of photosynthetic microbial communities was assessed in each microsite by the visible presence/absence of orange and/or green pigmentation, i.e., standard ocular estimate methods utilized in multiple previous studies^{23,32, 88,89,103,119}. Ocular estimates of the presence/absence of photosynthetic communities within the green and orange visible endolithic layers and biological soil crust³² were also further corroborated *in situ* with i) VSWIR and Raman instruments, and ii) in the Centro de Biotecnología's laboratory (e.g., Supplementary Fig. 2) with images and emission spectra with a wavelength λ -scan function of the Confocal Laser Scanning Microscopy (CLSM)¹⁰⁴ and with scanning electron microscope (SEM) according to the standards of the Centro de Biotecnología of the Universidad Católica del Norte and Geology Department of the University of Montana.

ES-2 (Habitats): Quantifying Photosynthetic Microbial Community Abundance and Habitats.

ES-2 was designed to investigate the effect of spatial variation of specific habitats on colonization. Classification of initial macro and microhabitat data from ES-1 was refined and a larger analytical scale of observation, the 'large-scale polygon/polygonal network,' was added with further UAV imagery analysis. It revealed that ridges and aeolian surface cover units comprised the exterior edges and interior surfaces, respectively of polygons at larger scales (1 to >30 m in diameter; Extended Data Fig. 1). Prior studies have shown these distinct types of network units (of all sizes) to influence biotic parameters or habitat geochemistry^{93,94,105}. In this regard, we quantified abundance in seven large polygons in ES-2 (5-35 m in diameter) and seven domes (1-5 m diameter) (Extended Data Fig. 2). For the large polygons, seven exteriors, i.e., ridges in ES-1, and seven polygon interiors, i.e., aeolian cover in ES-1, were mapped (n=147 total samples). In each habitat type, seven samples were randomly chosen and the following data collected: i) presence/absence of visible photosynthetic community biosignatures; ii) aspect/orientation of biosignatures (4 cardinal directions) and depth of colonized layers, if present; iii) microhabitat type(s); iv) samples for mineralogy and nutrient content; v) samples for gravimetric water content; and vi) samples for molecular biodiversity and biomarker profiling by multiplex immunoassays.

ES-3 (Fine-Scale): Dome, Ridge and Aeolian Cover Fine-Scale Studies.

In this third iteration, data and the rules and probabilities for biosignatures from ES-1 and ES-2 were further analyzed, refined, and tested as inputs and predictions in ES-3 (Extended Data Fig. 2). Microhabitat surface areas and photosynthetic biotic colonization were also mapped and quantified at much higher spatial resolution and detail to construct heat maps for fine-scale (cm to mm) habitats and biosignatures. Microhabitats were also further pre-characterized (and predictions generated) using ground-based VSWIR hyperspectral scans (see above methods) and assessments of panoramic visual imagery. Subsequently, for each macrohabitat unit 1-m² quadrats (5-cm grid n=400 samples per quadrat, Extended Data Fig. 2) were used to map, quantify and confirm fine-scale biosignature patterns. Macroscale habitat orientation was held constant by selecting unit areas adjacent to each other in the same orientation, thus controlling for macroscale climate variations including light, temperature and wind speed/direction. Visual and VSWIR hyperspectral panoramic and ground-based (i.e., hand-held camera) visual images of the ridge, dome and aeolian cover macrohabitats were also acquired to overlay onto biosignature data and assess microhabitat visual and spectral fidelity. Following co-located scans, in each 5 cm² sample, the following data were recorded: i) presence/absence of photosynthetic community biosignatures; ii) type of colonization (endolithic and/or BSC); iii) aspect/orientation of biosignatures (4 cardinal directions) and depth of colonized layers, if present; and iv) microhabitat characteristics (e.g., type, features, spatial location, presence of a transition, powdery consistency in crystals, proximity to vertical crack). Mineralogy and molecular biology samples were also collected. Data from ES-3 formed inputs for spatial statistical analyses and deep learning models.

Statistical Ecology and Deep Learning Methods

Microbial Landscape Studies (ES 1-2): Spatial and habitat effects on colonization

Chi-square tests for independence were conducted to assess differences in the ratio of colonization among the macro and microhabitats, and at each spatial scale (Extended Data Table 2).

Spatial Randomness/Aggregation Analyses (ES 1-3; Ripley's K, Global Moran's I)

Spatial statistics are a broad suite of statistical methods enabling the identification and comparative analysis of spatial patterns utilizing data that have a spatial characteristic^{85,106}. One such tool is Ripley's K function which is used to identify randomness and clustering of points within a spatial group^{85,106,107}. Ripley's K and Global Moran's I were used to assess spatial pattern at UAV and fine-scales for endolithic and BSC communities at Pajonales. Ripley's K analyses were conducted with R package *spatstat*^{108,109} using grid coordinates and presence/absence data for ES1-3. Permutation tests (999 random permutations) for Global Moran's I statistic of the same data were conducted with R package (<https://link.springer.com/article/10.1007/s11749-018-0599-x>). Spatial relationships were defined by inverse distance weighting (1/distance). For Results see Supplementary Fig. 3.

Deep Learning Methods

At the fine scale, the predictability of (endolithic/BSC) biosignatures, and the association with particular microhabitats (proxies for water availability), were analyzed with pivot tables (for rules) and tested for predictive power with convolutional neural networks (CNN, Fig. 5a-c) and spatial generalized additive models (GAM, Fig. 5d).

GAM Methods

Predictive model for endolithic colonization of dome macrohabitat

A spatial logistic generalized additive model (GAM) was conducted using the *mgcv* package in R (version 4.0.4) with a restricted maximum likelihood for the parameter estimation:

$$\log(p/1-p) = \beta_0 + \beta_1 T2 + \beta_2 T1 + f(x_coord, y_coord), \quad (1)$$

where p is the probability that the response variable (endolith, binary, 0-1) occurs in a cell^{110,111,112}. A smoothness function fx_coord, y_coord was included to account for the spatial coordinates x_coord and y_coord . Observations that are closer in distances will have a stronger correlation than observations that are further apart. The smoothness function was a bivariate P-spline.

Alabaster was not included in the model given that it was linearly dependent with endolith (correlation was close to 1) and inclusion in the model would have impacted the outcomes of other variables in the model. This was also observed for sand and float, which were both negatively correlated to endolith (close to -1) and thus were not included in the model.

The microhabitats considered in the model as binary outcomes (1=microhabitat exists, 0=does not exist) included Type I (T1) crystal microhabitat and Type II crystal microhabitat (T2). The model can be written as:

$$(p/1-p) = \exp(\beta_0 + \beta_1 T2 + \beta_2 T1 + f(x_coord, y_coord)), \quad (2)$$

where p is the probability of observing endolith and the term $p/1-p$ is referred to as the *odds ratio* or the likelihood of observing endolithic biosignatures given the presence of the microhabitat T1 or T2. Estimation and inference results related to the spatial logistic GAM in equation (1) are given in Supplementary Table 3. With this model, a probability contour map for endolithic life in the dome face macrohabitat was created (Fig. 5d, left box).

Predictive models for endolithic and BSC biosignatures in aeolian cover macrohabitat

Spatial logistic GAMs were also conducted, with a restricted maximum likelihood for the parameter estimation, to separately estimate the probability of endolithic and biological soil crust (BSC) biosignatures in the aeolian cover-macro habitat. Both models were formulated as follows:

$$\log(p/1-p) = \beta_0 + \beta_1 \text{ sand} + f(x_coord, y_coord), \quad (3)$$

where p is the probability that the response variable (endolith/BSC, both binary, 0-1) occurs in a cell and the term $p/1-p$ is the *odds ratio* or the likelihood of observing endolith or BSC biosignatures given the presence of sand. The same smoothness function described earlier is also included in eq. (3). Similar to the dome model above, alabaster was not included in the model given its linear dependency with endolithic colonization (correlation was close to 1) and inclusion in the model would have impacted the performance of other variables in the model.

Pivot Table and Decision Tree Methods

Pivot-tables count the number of events, where for Pajonales each event is some combination of microhabitat (e.g., alabaster, sand) and biosignature, as %Col (endolith, BSC). We derive a decision-tree from the pivot-table, in which the order of yes/no questions centered on a microhabitat is chosen to maximize the likelihood of detecting a biosignature in the fewest questions possible. Pivot tables and decision tree results are shown in Extended Data Fig. 3 and Supplementary Tables 1-2 and Fig. 4.

Convolutional Neural Networks (CNN) Methods

A CNN is a machine learning model that specializes in the isolation and extraction of salient features from spatial data in a data-driven manner¹¹³. That is, a feature is deemed salient if it is predictive of the target ground-truth. To create the model, optical data were taken *in-situ* with an iPhone 7 of the dome and aeolian cover macrohabitats and later split into 32 pixel by 32 pixel subsets and annotated for the following variables: microhabitat type and presence/absence of endolithic or BSC biosignatures. To quantify the effect of the split of the macrohabitat into mutually exclusive training, validation, test image chips, we train and evaluate the CNN model across 10 randomized splits (for examples, see Supplementary Fig. 7), and generated Recall-Precision curves per randomized split (see Recall-Precision curves in Supplementary Fig. 6).

Annotated images (four per cell in the 10x10 cell-grid) from each macrohabitat were split randomly into subsets of 70% training, 15% validation, and 15% testing, following standard best practices to avoid overfitting and prevent leakage of information between training and validation/testing datasets.¹¹⁴ After removing images with holes/no samples, 349 images remain in the dome macrohabitat and 378 images remain in the aeolian cover macrohabitat (Supplementary Fig. 8). Predictions on the training set were used to fit the CNN model parameters. Predictions on the validation set were *not* used to fit the model, but they were used to assess whether the model overfits the training data: if the training accuracy (defined as $[\text{true positives} + \text{true negatives}]/[\text{size of data set}]$) and validation accuracy numbers are similar, then no overfitting occurred. If overfitting occurs, it means that the model can predict only the ground truth of the training data by memorization, rather than distinguishing actual salient patterns in the imagery that are generally predictive across the entire macrohabitat. On the other hand, one can rely too much on the validation accuracy, such that it is now the model design (e.g., depth of the neural net) that is at risk of overfitting, but in this case on the validation set. Therefore, a third subset, the testing set, was used at the end of each randomized run to measure the final test accuracy of the model. In effect, an accuracy in the test set that is comparable to that of the validation set implies that the model design process was not contaminated by our assessments on the validation set. Therefore, we can conclude that the model generalizes across the entire macrohabitat. See Fig. 5 for results, and Supplementary Fig. 7 for examples of randomized image splits.

For pixel-wise classification of the study site and its surroundings a fully connected convolutional neural network, or fully convolutional network (FCN), was employed¹²⁶. The orthophotomosaics were split into 708 individual subframes approximately 18.5 x 18.5 m in extent for input into the FCN. We used standard data augmentation techniques of rotation, reflection, and illumination adjustments to increase the total data volume 18-fold for a total of 12, 744 images with ground truth labels. The images were split into training (75%), validation (12.5%), and testing (12.5%) datasets and statistics were drawn on the distribution of classes within each dataset to ensure consistency in the representation of each class across the datasets (Supplementary Fig. 5). We chose to split the orthophoto mosaic scenes into the following 11 classes: AeolianCover, MottledGround, PatternedGround, PolygonRidge, Dome, Objects and Road. Ground truth labels were created in a GIS program using the highest resolution orthophoto mosaic by a remote sensing geologist with on-the-ground knowledge of the field site. A version of the ResNet50 CNN⁴⁹ trained on over 1 million images from the ImageNet database was used as the network backbone for our FCN. Training was carried out on clusters on the Infrastructure for Scientific Applications and Advance Computing (ISAAC) facility at the University of Tennessee, Knoxville with an adaptive moment estimation (Adam) solver until the loss rate stabilized (typically < 40 epochs). We

calculated standard evaluation parameters Boundary-F1 contour matching score (BF-score), Precision, and Recall, as well as network uncertainty, which was used to formulate a “confidence score”. Network uncertainty was calculated using the Monte Carlo Dropout method (MC Dropout).¹²⁷ A confidence score was formulated as follows:

$$\text{Confidence Score (\%)} = (TP_i * TC_i + FP_i(100 - FC_i)) / N_i$$

Where TP_i and FP_i are true and false positives, respectively, for class i . TC_i and FC_i are the network certainty (0 - 100%) averaged over all true and false predictions, respectively, for class i , and N_i is the total number of pixels predicted as class i . Evaluation metrics are presented in Extended Data Table 4. While typical evaluation metrics for semantic segmentation, such as the BF-Score, measure how accurately a network draws a segmentation boundary around features, the Confidence Score reports the degree to which a user should trust the network certainty analysis for a given class. The Confidence Score metric, therefore, enables a more nuanced analysis of network results and feature identification than typical evaluation metrics. Confidence Scores can be high even if the boundaries drawn around objects are inaccurate (i.e., BF-Scores are low), and, conversely, Confidence Scores can be low even if BF-Scores are high. If the Confidence Score is high relative to the BF-Score, it means that the uncertainty analysis is reporting useful information upon which users should rely (i.e., the network is not confident about false predictions and is confident about true predictions); but if the opposite is true, users should be wary of the network certainty analysis because the network is likely overly certain of false predictions. Therefore, we report Confidence Scores values in the main text, but for relevant classes we report BF-Score, Precision, and Recall alongside Confidence Scores for reference (Extended Data Table 4).